

## Approaches to Optimization of Experimental Design for Cosmic Ray Mass Composition Studies in the 1–1000 PeV Energy Range

D. V. Chernov<sup>1\*</sup>, C. J. Azra<sup>1,2</sup>, E. A. Bonvech<sup>1</sup>, O. V. Cherkasova<sup>1,3</sup>,  
E. L. Entina<sup>1</sup>, V. I. Galkin<sup>1,2</sup>, V. A. Ivanov<sup>1,2</sup>, T. A. Kolodkin<sup>1,2</sup>,  
N. O. Ovcharenko<sup>1,2</sup>, D. A. Podgrudkov<sup>1,2</sup>, T. M. Roganova<sup>1</sup>, and M. D. Ziva<sup>1,4</sup>

<sup>1</sup>*Skobeltsyn Institute of Nuclear Physics, Moscow State University, Moscow, 119991 Russia*

<sup>2</sup>*Faculty of Physics, Moscow State University, Moscow, 119234 Russia*

<sup>3</sup>*Department of Cosmic Space, Moscow State University, 119991 Moscow, Russia*

<sup>4</sup>*Faculty of Computational Mathematics and Cybernetics, Moscow State University, Moscow, 119234 Russia*

Received September 1, 2024; revised September 1, 2024; accepted September 3, 2024

**Abstract**—The new SPHERE-3 detector is under development. The main purpose of this experiment is to study the mass composition of primary cosmic rays in the energy range of 1–1000 PeV. The difference between this detector and the previous ones in this series is the registration of not only the Cherenkov light reflected from the snow, but also direct light entering the detector. Several options are being considered for recording direct Cherenkov light. The article presents the estimated parameters of the optical scheme of the detector and the first estimations of its sensitivity to the energy and mass of the primary particle. The first approximations of methods used for energy and mass of the primary particle assessment in each event are given, and their accuracy is considered. At the moment, methods for reflected Cherenkov light and direct Cherenkov light processing are being considered independently of each other.

**DOI:** 10.1134/S1063778824700959

### 1. INTRODUCTION

The project is aimed at studying the energy spectrum and nuclear composition of primary cosmic rays (PCR) in the energy range of 1–1000 PeV. There are indications that a significant part of PCR nuclei with energies from 100 to 1000 PeV may have an extragalactic origin [1]. The study of the composition of PCR at these energies may be of decisive importance when choosing a model for the transition from galactic cosmic rays to extragalactic ones, what, in turn, is important for the construction of a global picture of acceleration and propagation of cosmic rays. The problem of mass composition of primary cosmic rays of ultrahigh energies ( $E > 1$  PeV) is currently far from its final solution [2–5]. The KASCADE-Grande experimental group was able to isolate the spectra of two groups of nuclei [6–8], a more detailed classification is hindered by the uncertainty of the strong interaction model. Despite several decades of research focused on measurement of the composition of PCR by indirect methods using components

of EAS and dozens of experiments conducted, partial spectra of whole groups of nuclei have not yet been measured. Moreover, the results of various experiments on the average logarithm of the mass number in the energy range of  $\sim 10$  PeV differ by several times [5–11]. The attempt to create a global model of partial spectra (Global Spline Fit, GSF) in a wide range of primary energies [12] rests on the absence of systematic errors in some experimental groups and suffers from uncertainties in the model of nuclear interactions, therefore it can only be perceived as a call to continue research. Meanwhile, a good knowledge of the partial spectra of groups of nuclei is necessary for testing various models of acceleration and propagation of PCR. Therefore, new experiments sensitive to the nuclear composition of cosmic rays are very important for modern astrophysics.

The idea of the new SPHERE-3 system arose on the basis of our previous experience in solving the problem of the mass composition of PCL and registering a double Cherenkov signal (reflected from snow and direct) from a real EAS with the SPHERE-2 telescope [13]. The experience of calculations done for the Cherenkov part of the Pamir-XX project [14]

---

\*E-mail: chr@dec1.sinp.msu.ru

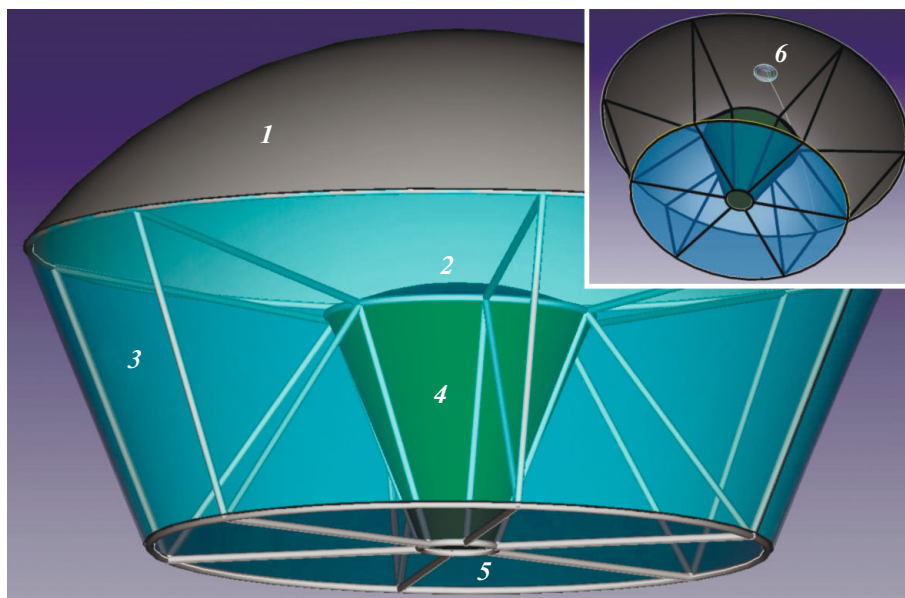


**Fig. 1.** The design of the SPHERE-3 detector. Highlighted elements are: 1—a spherical mirror, 2—SiPM camera, 3—lens hood, 4—an electronics unit, 5—corrector plate, 6—direct Cherenkov light detector.

was also used. It demonstrated the high potential of the angular distribution of Cherenkov light for separating EAS by the mass of the primary particle and the special information requirements of the PCR mass composition studies. In order to achieve the best accuracy in estimating the primary mass, it was decided to optimize the new setup specifically for this task. Optimization should be carried out by thorough statistical modeling of artificial events, the process of their registration with new detectors and sufficiently complete data processing of this numerical experiment. A number of detector design options have already been considered and a method for comparing their quality in terms of solving the task has been chosen.

At the moment, the search for shower parameters sensitive to mass is underway. These parameters differ for direct and reflected Cherenkov light. For the reflected light detector, the mass parameter is the shape of the Cherenkov image. The length of the large axis of the image is currently used in the direct light detector, but we expect to find a more sensitive parameter. Several design options for both detectors are currently being considered. The quality of each of the variants is evaluated by solving the classification problem for samples from several primary nuclei. The numerical quality indicator is the classification error of each of the nuclei.

In the end, with already defined mass sensitive parameters and selected detector design, it is assumed to set and solve the regression problem, that is, the algorithm will estimate the primary mass of each event. As a result the overall experimental scheme

optimization (telescope design, experimental strategy, trigger conditions and processing algorithms) for the problem of the PCR mass composition should give minimal errors in mass estimates. In the process of searching for primary mass sensitive parameters a simpler classification problem is solved: for each candidate parameter the boundaries are calculated (the critical values of the parameter separating adjacent classes) and the corresponding classification errors, using samples of artificial events from protons, nitrogen and iron nuclei. These errors allow us to evaluate the quality of both the parameter under test and the entire experimental scheme as a whole.

Along with the primary mass, other primary parameters are estimated: arrival direction and energy. The reflected light telescope allows to estimate the energy, direction, mass and position of the axis on the snow. The direct light detector measures the angular distribution and has a small area, so its functions include only estimating the direction and mass.

## 2. THE SPHERE-3 DETECTOR AND ITS PROTOTYPE

### 2.1. Detector Design and Optical Scheme

In Fig. 1 the design of the SPHERE-3 detector is shown. A sturdy metal frame connects all elements of the optical system: 1—mirror, 2—SiPM based camera with 4—measuring equipment, 3—lens hood for cutting off side illumination, 5—corrector plate. In the partially shaded by the mosaic central area of the mirror a direct Cherenkov light detector 6 can be installed.

**Table 1.** Detector parameters of SPHERE-2, SPHERE-3 and its prototype

Parameter	SPHERE-2	Prototype	SPHERE-3
Aperture (effective), m <sup>2</sup>	0.5	0.16*	2.27 (1.33)*
Mirror diameter, mm	1500	800*	2200*
Viewing angle (effective), degree	±26	±23*	±23 (20)*
Number of pixels	109	300*	2–3 × 10 <sup>3</sup> *
Detector mass, kg	90	15*	100*
Maximum flight altitude, m	up to 900 (balloon)	up to 500 (UAV)	up to 2000 (UAV)

\* Preliminary.

The main characteristics of the SPHERE-3 detector are shown in Table 1. For comparison, characteristics of the SPHERE-2 detector and the proposed prototype of the new detector are also given. Experience of creating and operating the SPHERE-2 detector was taken into account in the development of the SPHERE-3 telescope. To simplify the design and assembly of the new detector, the electronics unit was located directly behind the SiPM mosaic (see Fig. 1). This was made possible by the small size of the SiPM and the use of multi-channel FADCs (see section “SiPM segment”). This arrangement of the electronics unit does not reduce the aperture since it is in the shadow of the mosaic itself (no light that can be reflected from the mirror to the sensitive elements passes through this volume). In addition, cable lengths are minimized and, accordingly, signal attenuation from SiPM is minimized. Fans are placed in the lower part of the electronics unit to remove heat through an opening in the center of the diaphragm inlet window.

The SPHERE-3 telescope uses a Schmidt optical system with a corrector plate. In order to reduce the spherical aberration effects and increase optical resolution, the corrector plate and mirror both have aspherical surfaces. In Fig. 2 the resulting optimal optical scheme parameters are shown. As can be seen from the figure, the characteristic diameter of the light spots was about 10 mm for paraxial light beams within a  $\pm 20^\circ$  cone. Such a spot diameter is an optimal compromise for a SiPM mosaic with a similar distance between the pixels' centers. I.e., the optical resolution of the light collection system and the spatial resolution of the mosaic are close. Despite the fact that the shapes of the spots on the SiPM mosaic differ at different light arrival angles, the integral values (energy within a certain spot radius) are close to each other and amount to about 80% within a 5 mm radius. In addition, the figures show that the light spectral components do not significantly differ

in spot shapes, given that the maximum sensitivity of the SiPM is in the region of 420 nm.

The prototype of the SPHERE-3 telescope has smaller dimensions (see Table 1), but completely repeats the design and allows to implement the full functionality of the main detector. The prototype is necessary in order to test the elements of the photodetector and electronics, including measuring boards, trigger, information acquisition system and detector control systems. All these elements of the equipment after testing and commissioning will be used in the SPHERE-3 telescope without significant changes.

Same as the main detector, the prototype has a Schmidt optical system (see Fig. 3). The aim of the prototype elements' development was to obtain a similar optical resolution of around 10 mm in order to use the same SiPM segments as the main detector. In Fig. 3 the results of this effort are shown. It was possible to obtain similar-shaped light distributions for a camera mosaic about 7 times smaller. I.e., one pixel of the mosaic of the prototype approximately corresponds to a segment of 7 pixels of the SPHERE-3 camera.

## 2.2. SiPM Segment

In Fig. 4 the main element of the SPHERE-3 camera, one of seven silicon photomultipliers (SiPM) is shown. Several variants of SiPM with a sensitive area of 6 mm × 6 mm are being considered: MicroFC-60035, MicroFJ-60035, JSP-TP6050, EQR20 11-6060.

In this project, it is planned to refine and adapt the previously developed SiPM segment for use with a new optical system. The preamp system will have to ensure the passage of long-duration signals—up to several hundred nanoseconds, and the light collector system should concentrate photons coming from the mirror with angles up to  $\pm 60^\circ$  or even more. Lens light collectors are capable of providing such a large angle of light collection. Preliminary measurements

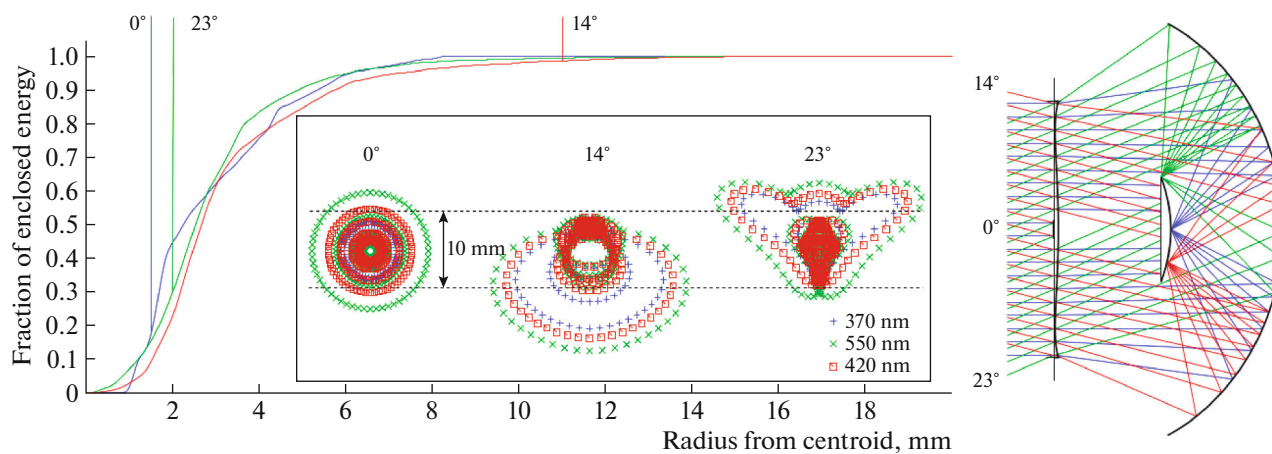


**Fig. 2.** A preliminary version of the SPHERE-3 detector optical system. The graph on the left shows the fraction of collected light depending on the radius of the collection spot for different light incidence angles ( $0^\circ$ ,  $14^\circ$ , and  $23^\circ$ ), and the light spot's shape (wavelength of 370, 420 and 550 nm). On the right: detector optical scheme.

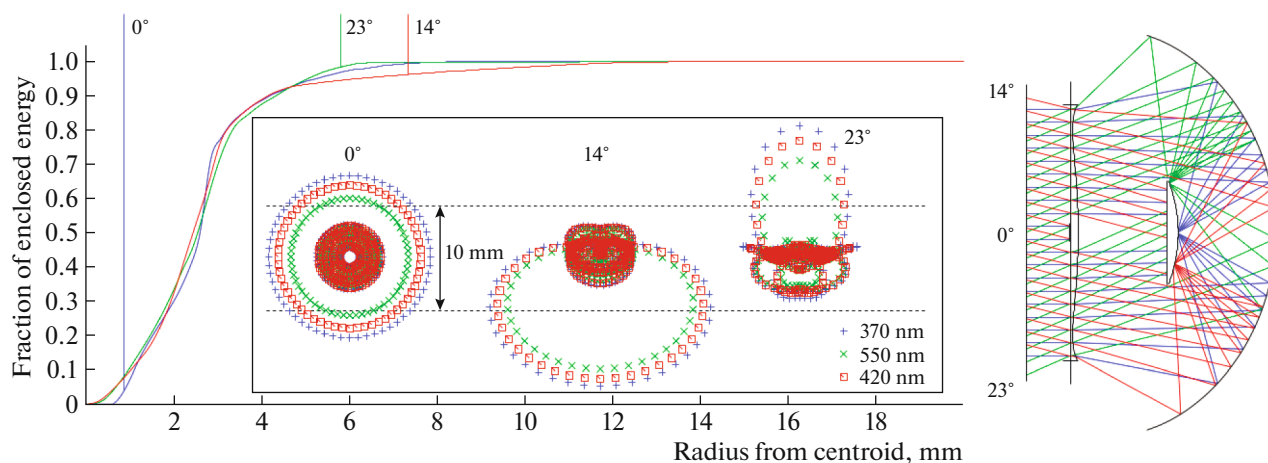


**Fig. 3.** A preliminary version of the SPHERE-3 detector prototype optical system. The graph on the left shows the fraction of collected light depending on the radius of the collection spot for different light incidence angles ( $0^\circ$ ,  $14^\circ$ , and  $23^\circ$ ), and the light spot's shape (wavelength of 370, 420 and 550 nm). On the right: detector optical scheme.

with ready-made, commercially available spherical lenses with a diameter of 12.5 mm with a curvature radius of 8 mm showed an increase in light collection by 2.5 times from angles of  $60^\circ$  or more from the optical axis. It is planned to develop more effective lenses for the new SiPM segment.

### 2.3. Measuring Channel Electronics

For measuring the profile of analog SiPM signals a digitization board based on an 8-channel fast analog-to-digital converter (FADC) will be used. ADS5294 or similar chips are considered as FADCs. These chips operate at 80 Ms/s (e.g. 12.5 ns interval) with a digitization resolution of 14 bits. Since the segment consists of 7 SiPMs, the eighth channel can be used to increase the digitization frequency for the central

segment's pixel by 2 times to 160 MHz. In this case, an additional channel is connected via a short delay cable. In the future, it is planned to use the interpolation method to restore the shape of the pulse in the channels adjacent to the central one. Digitized signals from each channel through a delay line are sent to a programmable logic chip, where they are continuously recorded in the 1st level buffer memory with a depth of up to 12.8 microseconds. When the "trigger confirmation" signal arrives, the data enters the 2nd level buffer memory, where it is stored until it is read and written to external media (an SD card). The data from the measuring channel FADC is sent in parallel to the buffer (through delay line) and to the data preparation unit for the trigger. The preparation unit is a "running sum" integrator that forms the sum of the last few input values. The number of summed

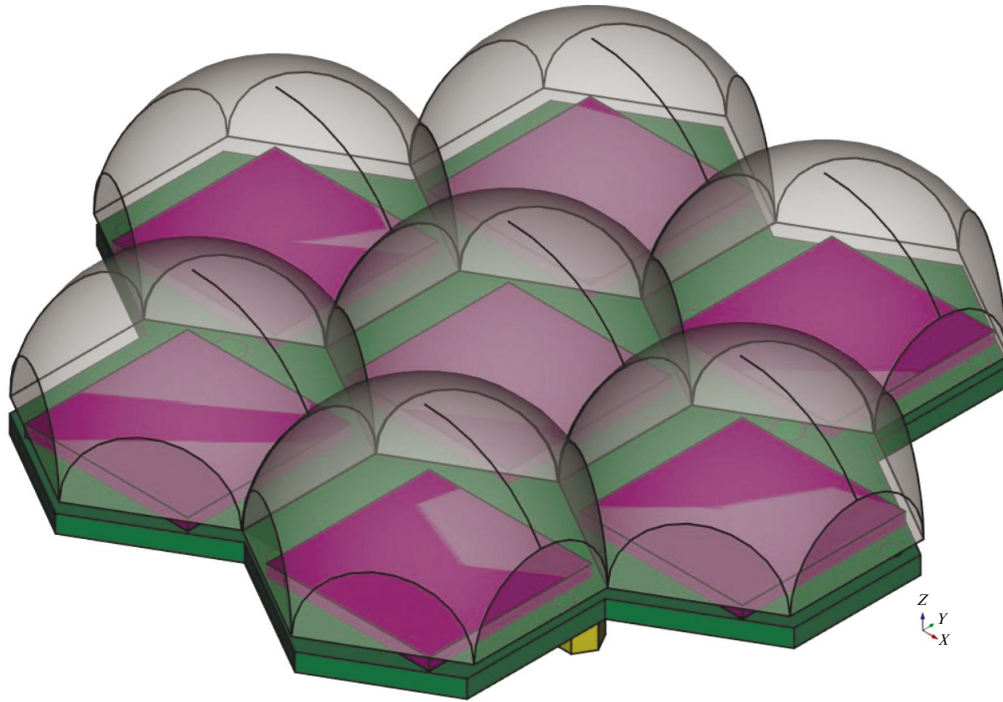


**Fig. 4.** Preliminary version of a SiPM segment with lens light collectors. Full SiPM size of  $7 \times 7$  mm (the image does not reflect real light collector properties, those are given as an illustration only).

values can be from 1 to 16 depending on the settings. The preparation unit continuously sends packets to the trigger with 1 or 0 for every pixel whose running sum does or does not exceed a specified threshold. The threshold value is set before the start of detector operation.

The measuring channel boards are equipped with an integrated computer running on the Linux operating system. All measurement data is stored on a built-in SD card in the form of packets with a number and a timestamp. The timestamp is generated by the trigger board when each trigger confirmation signal is generated. After the measurements are completed, all data from the measuring boards is read to an external computer via an Ethernet port for subsequent clustering and formation of individual event files. Such an organization of data collection allows to significantly increase the data collection speed and reduce the detector's "dead time".

#### 2.4. Trigger

The trigger board receives signals from discriminators from each measuring channel. To reduce the number of cables, the signals are transmitted in packets from each SiPM segment. Accordingly, the total number of trigger board inputs can be reduced to less than 400, what means that only one programmable logic chip can be used to implement any specified trigger conditions. The data transmission

bus frequency for packets is 10 times higher than that of the measuring channels' ADCs. The condition for the trigger board to broadcast a trigger confirmation signal that initiates data recording is the simultaneous activation of two or more adjacent pixels. The layout of all pixels is loaded as firmware into the memory of the trigger chip before the start of operation. The trigger confirmation signal is transmitted back to the electronics of the SiPM segment via the same bidirectional line along which the trigger receives the data from the channels. The segments wait for the confirmation signal after data transmission from the channels. Thus, it is possible to transmit the trigger confirmation signal not to all segments, but only to those that house activated pixels and those that are adjacent to them. This allows to significantly reduce the total amount of information stored. When the trigger confirmation signal is received, the segments save an oscillogram with the SiPM signal profile to the SD card. The stored data is taken from the delay line so the stored signal contains data for some time before and after the trigger confirmation signal arrives.

### 3. MODELLING

Optimization of the new detector designed for the task of PCR mass composition studies [15] requires the accumulation of a database of artificial events for

a multidimensional set of primary parameters (primary energy, type, arrival direction) and models of the atmosphere and nuclear interactions. The CORSIKA package [16] was used with custom output files. Specifically, information about charged particles was not stored, and data on the characteristics of Cherenkov photons was stored in the form of multidimensional arrays. This approach allowed: 1) to make the database as compact as possible, what was impossible with the standard version of CORSIKA, and 2) to use artificial events repeatedly simulating different detector positions relative to the EAS core.

The main observation level corresponds to the altitude of the Lake Baikal ice surface. At this level, an array of the spatial and temporal distribution of Cherenkov photons was recorded in each event on an area measuring  $\sim 10 \text{ km}^2$  centered on the shower axis, paved with  $2.5 \text{ m} \times 2.5 \text{ m}$  squares. Photon arrival times were tracked relative to the shower plane within 500 ns with 5 ns steps. Additionally, combined spatial, temporal and angular photon distributions were recorded at three more altitudes. Initially they were 500, 1000 and 2000 m above the observation level. Currently the maximum altitude has been reduced to 1500 m. The spatial grid was rectangular in the range from  $-200 \text{ m}$  to  $200 \text{ m}$  at both coordinates in increments of 10 m, the angular grid was also rectangular ranging from  $-25^\circ$  to  $25^\circ$  relative to the vertical axis with  $1^\circ$  grid step, the time grid was defined in the range 0–64 ns in increments of 2 ns plus an integral cell to account for late arriving photons.

To solve the methodological problems associated with using the angular distribution of Cherenkov light, in particular, to analyze its information capabilities, other options of the angular grid were considered for modeling. For this 120 showers for three primary nuclei (proton, nitrogen and iron) with two energies (10 and 30 PeV) and a zenith angle of  $15^\circ$  were simulated using each of the intermediate grids (“fine” and “superfine” with  $0.5^\circ$  and  $0.25^\circ$  grid steps respectively) and the new “super-superfine” grid ( $0.2^\circ$  step). Analysis of these samples allowed us to choose the main version of the angular grid for further simulations—the angular distribution is recorded by CORSIKA in a square area from  $-15^\circ$  to  $15^\circ$  relative to the direction of the shower axis along both coordinates with a step of  $0.2^\circ$ .

The simulation of reflected Cherenkov light images in the main telescope was divided into two stages. First, based on the spatial–temporal distributions from the CORSIKA simulation, photons are traced to the entrance window of the telescope. Then these photons are traced through the optics of the telescope until their absorption or exit through the detector’s entrance. The set of photons that were absorbed by SiPMs form the images that then end

up in the corresponding database of reflected light events.

Each EAS event contains spatiotemporal light distribution for the observation level, which allows it to be used many times for different positions of the shower axis relative to the detector. We refer to this procedure as “event cloning.” An independent image of reflected light from each clone in the telescope is obtained. Usually 100 clones for each event were considered.

Similarly, direct light images are obtained by drawing a set of photons from the angular distribution of photons corresponding to the considered flight altitude and the position of the detector relative to the shower axis. Then these photons are traced through the same direct light detector model (same as described above for the main camera detection option or through a separate model for the dedicated direct CL detector). Sets of photons then form images that are stored into the database of images of direct light.

The tracking of optical photons through both detectors is done by applications based on the Geant4 package that reproduces the detectors’ structure fairly accurately.

The angular distributions of Cherenkov light are also cloned. In this case, the event for a given detector position relative to the shower axis is represented by a sufficiently detailed two-dimensional angular histogram, the contents of which are interpreted as probabilities of receiving a photon coming from the corresponding direction. From these cloned distributions, images are further obtained in a direct light detector.

The generated images of direct and reflected light are then accumulated into a general database for further use (in the data processing and analysis of algorithms’ construction, configuration and tuning, which also includes joint processing procedures for double detection).

### 3.1. Reflected Cherenkov Light Detector Model

The detector’s optical scheme (Schmidt camera) was modeled and optimized in the ZEMAX package. This scheme includes an aspherical mirror (unlike SPHERE-1 and SPHERE-2), a corrector plate and a mosaic of optical modules with lens light collectors. For the purposes of the project two approaches to the optical scheme design were chosen: (A) a scheme with a maximized aperture and (B) a scheme with a maximized viewing angle. The natural limitation in both schemes is the diameter of the mirror, for technical reasons its diameter cannot exceed 2200 mm. The parameters of the schemes are given in [17].

Optimization of the optical scheme was carried out in two stages: first, light collection on the optical

surface of the camera was optimized, then, the shape and position of the light collector were optimized for better light collection on the SiPM.

Cherenkov photons were tracked in the telescope using the GEANT4 package with a detector model which corresponds to the optimized scheme modeled earlier in ZEMAX. Since GEANT4 does not have special methods for working with geometries of this complexity level, it was decided to use the CADMesh library [18] and import geometry elements in the STL format.

Logically, the following elements involved in optical calculations are highlighted in the model:

1. Corrector plate (an aspherical lens);
2. Back body of the SiPM camera (absorbs light);
3. Blend (absorbs photons);
4. Aspherical mirror;
5. Light collector over the SiPM;
6. SiPM plate (if a photoelectron hits it—registration is considered successful).

The detector model also includes a simulation of the electronics' response. The parameters of electronics operation were obtained by analyzing the operation of the prototype's optical module as part of the small wide-angle telescope SIT prototype [19, 20]. It is assumed that the electronics of the new detector will operate at the same frequency of 80 MHz, but with a higher digitization depth (14 bits). The response parameters of the SiPM and the amplification cascade were taken from an earlier work [17]. In the process variable SiPM parameters were taken into account: power supply voltage and temperature, which allows to accurately account for gain fluctuations and crosstalk (through a simplified Monte Carlo response model). Effects observed during the analysis of the SPHERE-2 electronics operation were also included in the simulation. This includes the presence of a nonzero signal baseline (associated with the specifics of the FADCs selected for use) individual in each pixel, the noise of this pedestal, the phase shift of the digitization moment in each module, etc.

At the output of the response simulation program, a file is obtained containing the closest format to the output of real equipment.

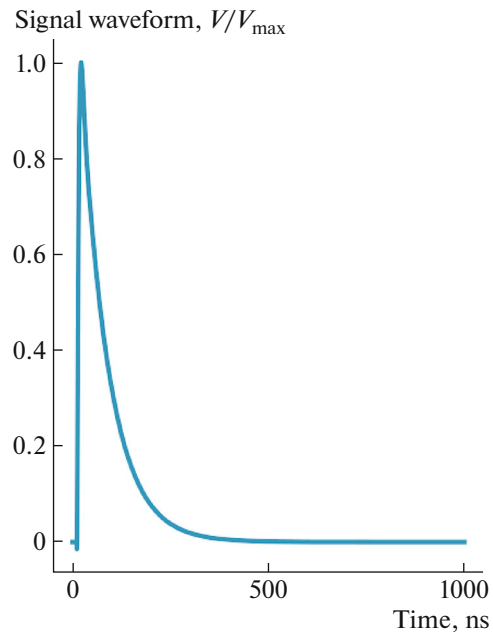


**Fig. 5.** An example of a normalized electronics response function to a single photoelectron. The shape of the pulse does not depend on pulse amplitude in our conditions.

### 3.2. Two-Stage Trigger Model

Since photosensitive elements of the new detector are subject to crosstalk, there is a need for additional filtering of events stored after the first stage (see “Trigger” section above). For each saved section of the recorded signal, it is necessary to determine whether there is an EAS signal on it, or only noise fluctuations, i.e. it is necessary to solve the classification problem.

Development of an additional image filtering method required auxiliary data preparation. To this end, an additional step was added to the procedure described in (Section “Modeling” above)—a set of example output signals was formed. Some sections contained signals with event photons and some were filled with background photons only.

Simulations of the detector response were done with the following parameters: SiPM voltage 29.6 V, their operation temperature  $-15^{\circ}\text{C}$ , background photon flux 0.013 photons per nanosecond per pixel. Impulse response of the SiPM used for modeling is shown in Fig. 5.

To form a set of example events a small number of events were selected from the database (QGSJETII-04 nuclear interactions model, CORSIKA atmospheric model No. 1, primary particle—iron nuclei with 10 PeV primary energy and  $15^{\circ}$  zenith angle). Then a fixed-length section of 50 bins (625 ns) was cut from the continuous recording of each generated signal. The beginning of the section was chosen

**Table 2.** Convolutional neural network architecture

Layer type	Parameters
conv2d	(1, 2, 3 × 3, 1)
conv2d	(2, 6, 4 × 4, 2)
conv2d	(6, 3, 4 × 4, 2)
conv2d	(3, 3, 4 × 4, 4)
dense	(345, 2), bias

**Table 3.** Classification results

		Detected as	
		event	noise
Real input	event	97.2%	2.8%
	noise	0.1%	99.9%

randomly 0–5 bins before the first event photon hit the mosaic. In addition, the same number of sections similarly with a length of 50 bins but containing only fixed-amplitude background photons were collected.

To solve the classification problem, a convolutional neural network consisting of 4 convolutional layers and a fully connected one was used. Network parameters and learning process settings are shown in Table 2. The main goal of this stage was to reduce the false positives rate (FPR), so that after training the neural network, additional fine-tuning thresholds could be set at its outputs, minimizing FPR. The results of the final version of the filtering algorithm is shown in Table 3.

As can be seen from Table 3, such an implementation of the second stage of the trigger mechanism makes it possible to reduce the number of false positives by 103 times, while sacrificing only 3% of events for the energy of 10 PeV. This in turn allows to set the initial pixel thresholds (see section “Trigger”) lower so as to reduce the detector energy threshold.

## 4. REFLECTED CHERENKOV LIGHT

### 4.1. EAS Energy Estimation

The energy is estimated based on the dependence of the full number of Cherenkov photons that reached the detector camera on the distance  $R$  on the snow from the shower axis to the center of the detector’s field of view. This number is obtained as an integral of the photon density approximation. Such dependencies (i.e.  $Q(E_0, R)$ ) can be obtained as a regression over the precalculated model values for different parameters (energies, angles, atmosphere

conditions). Energy estimates are made by measuring the full integral of the function approximating the image of a real event— $Q_{\text{exp}}$  and the reconstructed distance  $R_{\text{exp}}$ . A reverse interpolation can be used over the set of mentioned dependencies to obtain  $E_{\text{est}} = E_0(Q_{\text{exp}}, R_{\text{exp}})$ .

To assess the errors of the method, simulated EAS from primary protons, nitrogen and iron nuclei with energies of 5, 10 and 30 PeV were used. For each nucleus and energy, 11 events were modeled with 100 clones for each event. In total, 9900 events were analyzed with a uniform distribution of the axis points of incidence on the snow surface in a circle with a radius of 500 meters. A selection criterion has been introduced for clones: the distance from the center of the mosaic to the maximum point cannot exceed the size of the mosaic (325 mm) and the sum of square residuals cannot exceed a certain value. Also the mean square of residuals should not exceed a predefined threshold.

Photon distribution over the pixels was approximated by a function from [21]:

$$f(r) = \frac{p_0^2}{(1 + p_1 r + p_2 r^2 + p_3 r^{1.5})^2 \times (1 + p_4 r^s)}, \quad (1)$$

where  $r$  is the distance from the maximum and  $p_i$  are the free parameters.

In order to obtain better approximation results and selection criteria, the normalization coefficient  $p_0$  and its effect on the remaining coefficients of the approximating function were studied. However, no dependencies were found.

Dependencies of the average total photon counts  $Q(E_0, R)$  on the distance  $R$  are shown in Fig. 6. for several nuclei of different energies. To estimate the energy of an EAS primary particle of an unknown mass, three obtained dependencies for the same primary energy were approximated by a linear function. The EAS energy estimation then was done by putting the data from the test shower into this function. Due to the observed expected dependence of the shower brightness of the primary mass, a systematic shift will occur in primary energy estimation. To estimate the relative fluctuations, squares of 120 m × 120 m were taken along the  $X$  axis. The center of the first square lay at (0, 0), the second was at (120, 0), etc. The variation of mean in these squares was expected to be low based on previous results. The dependences of the relative fluctuations of the total photon count for the same three nuclei and same three energies are shown in Fig. 7.

The energy estimation errors from the described above procedure (shown in Fig. 6) are the smallest for

the primary nitrogen nuclei simply because the average of the three nuclei from Fig. 8 gives a dependence close to that of nitrogen. Therefore, in case of an unknown mass of the nucleus, the errors for protons and iron are the extreme ones and should be used as a tool to assess the energy estimation procedure accuracy.

In the future, the mass of the primary particle will be estimated for each event. It is also planned to improve the criteria for clone selection and their approximation. This will reduce the energy error, even if the mass is not determined accurately.

#### 4.2. EAS Axis Location and Arrival Direction Estimation

EAS axis location and orientation estimation was carried out on samples of artificial events from 10 PeV showers with a zenith angle of  $15^\circ$  and random azimuth directions from three primary nuclei ( $p, N, Fe$ ) for two telescope altitudes: 500 and 1000 m and without account of the night sky background and electronics response.

The simulated event was selected for analysis if the maximum amplitude of the signal summed over all measuring channels exceeded the threshold (40 photons), the length of the total pulse was within the time range [100–2000] ns, and the measuring channel containing the largest number of photons was not located on the last ring (see Fig. 9).

The EAS axis location was estimated as the center of mass of the two rings around the measuring channel that contained the most photons. If this channel was located on the penultimate ring, the axis was located as the center of mass of one ring around the brightest channel (Fig. 9). The distribution of errors in the axis localization is shown in Fig. 10a.

The EAS arrival direction was determined by approximating the shower front on the snow by a quadratic function. This was done in several stages. At the first stage, the signal in each measuring channel was isolated. The signal was searched in each individual channel by the sliding window method. The position of the window with the largest sum corresponds to the shower location. Due to the detector design in neighboring channels the signals from the EAS Cherenkov light overlap in time or are very close to each other. Thus, the EAS signal was searched for through adjacent channels starting from the brightest one. The average arrival time of the photons in each channel was taken as the arrival time of the EAS. Since the photon distribution is rather smooth each channel with a non-zero number of Cherenkov photons should have at least two adjacent channels with photons. If the channel was isolated then it was excluded from analysis as a fluctuation.

The resulting shower front on the mosaic consisted of a set of space–time coordinates  $x_i, y_i, t_i$ , where  $i$  is the number of the measuring channel. Then these times were reprojected onto the snow to account for time delays due to differences in optical path lengths.

The translation of time coordinates was carried out by subtracting the time path traveled from the snow to the mosaic. The coordinates of the measuring channels are translated by recalculating the coordinates of a point on the mosaic to the snow according to the dependence  $R = 5.53r$ , where  $R$  is the coordinate on the snow in m,  $r$  is the coordinate on the mosaic in cm.

The EAS front on the snow was approximated by the weighted least squares method. The weight corresponds to the amplitude of the signal. The equation approximating the quadratic function of the shower front:

$$t_{\text{fit}} = a_0 + a_1 R(\phi, \theta) + a_2 R^2(\phi, \theta), \quad (2)$$

where  $\phi$  and  $\theta$  are the zenith and azimuth angles respectively,  $R$  is the distance from the axis of the shower,  $a_0, a_1$  and  $a_2$  are the free parameters.

EAS arrival direction estimation errors were on average between  $1^\circ$ – $2^\circ$  (see Fig. 10). For the telescope altitude of 500 m the results are 25% better.

#### 4.3. Primary Particle Mass Estimation Using Reflected Cherenkov Light

To assess the quality of the detector geometry, it is necessary to process the received events and create criteria by which a certain geometry can be distinguished from others. The main goal of the SPHERE-3 detector is to refine the mass spectrum of the PCR, based on this, the evaluation criterion should be aimed at the quality of the PCR mass determination from the image on the detector mosaic.

As for now a method has been developed to estimate the mass composition of cosmic rays with energies of 1–100 PeV for the SPHERE-type detectors [21]. There is a software implementation of this method for the SPHERE-2 detector, it has been finalized and used again for the SPHERE-3 detector.

In this paper, the latest version of the Cherenkov photons lateral distribution function (LDF) approximation is used, which is described in detail in article [21]. In Fig. 11 an example of the distribution and its approximation are shown. The difference lies in the fact that in this work a one-dimensional criterion was used to test the possibility of primary mass differentiation based on the LDF projection on the mosaic.

It is known from calculations that the lateral distribution of Cherenkov light correlates well with the longitudinal development of the shower, therefore, a

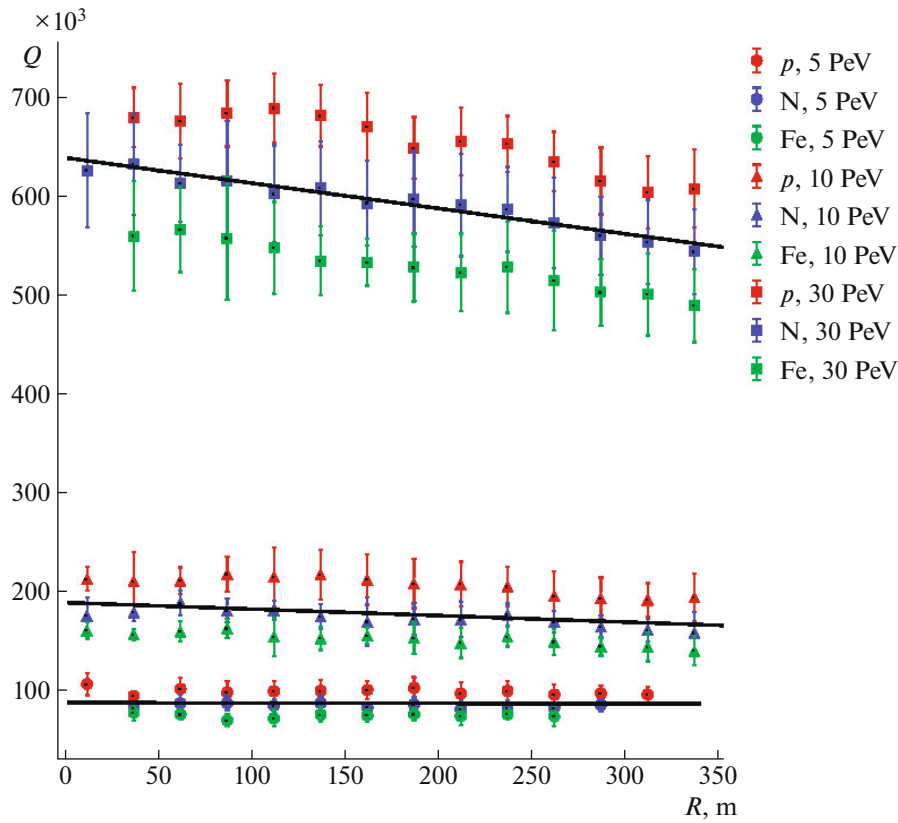


**Fig. 6.** The dependence of the total photon count  $Q(E_0, R)$  on the detector camera on the distance from the center of the detector's field of view to the shower axis for primary protons (red), nitrogen (blue) and iron (green) with energies of 5, 10 and 30 PeV (circles, triangles and squares correspondingly).

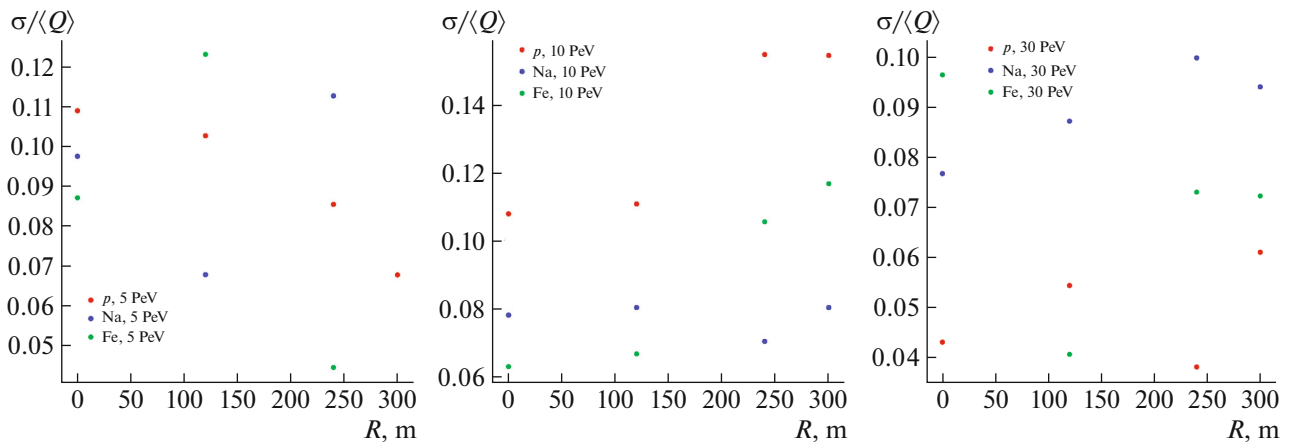


**Fig. 7.** Dependence of relative fluctuations on the distance from the center of the detector's field of view for protons (red), nitrogen (blue) and iron (green) of 5, 10 and 30 PeV.

dimensionless parameter was found which characterizes the shape of this distribution and can be calculated from the directly measured Cherenkov image. Another requirement for the criterion was its integrality: it must rely on a significant proportion of the light contained in the spot, what is important from the point of view of fluctuation suppression in both signal

and noise. Finally, the criterion should be weakly dependent on the strong interaction model. Relative criteria based on the parameters of the distribution form, but not on its absolute characteristics, have all of the above mentioned properties.

For this work showers with a  $10^\circ$  zenith angle from 10 PeV primary protons, nitrogen and iron nu-

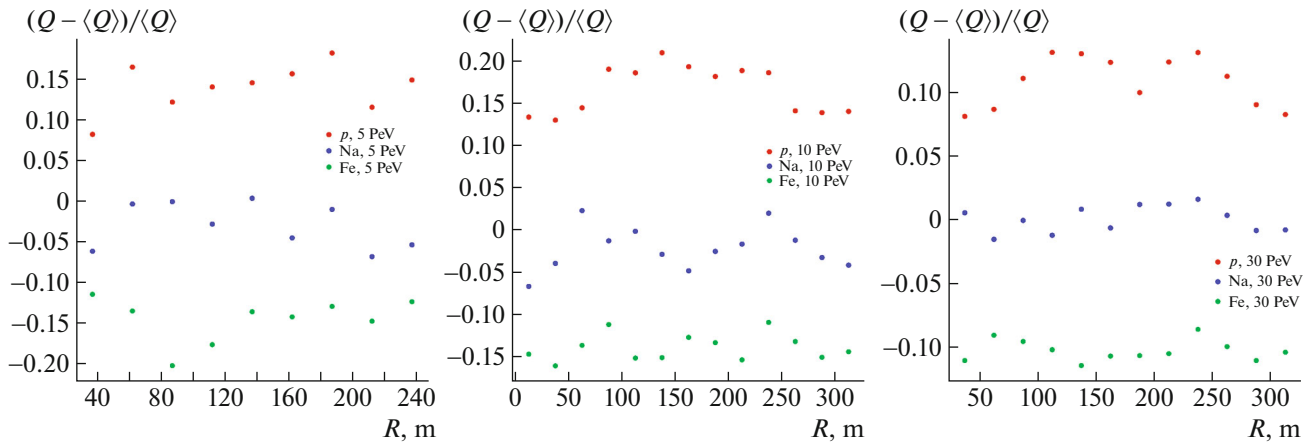


**Fig. 8.** Dependence of relative energy estimation errors on the distance from the center of the detector’s field of view for protons (red), nitrogen (blue) and iron (green) of 5, 10 and 30 PeV.

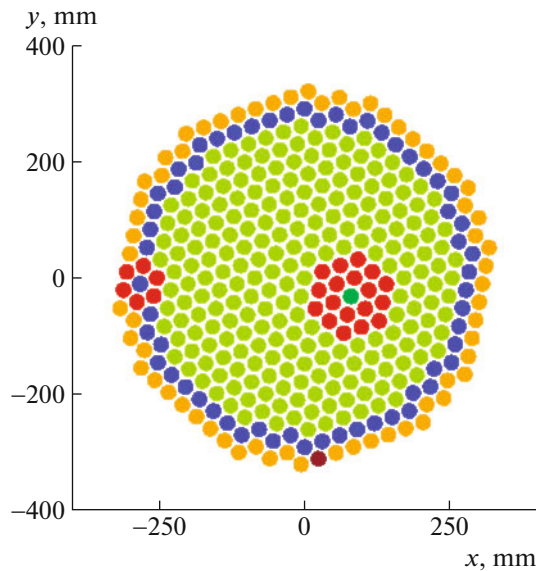


**Fig. 9.** Examples of rings used in the axis location procedure.

clei were used. The detector altitude was considered 1000 m. A one-dimensional criterion was constructed as a ratio of LDF integrals in the central circle ( $r_1$  radius) and in the ring with  $r_1$  inner and  $r_2$  outer radii. The outer radius  $r_2$  was limited to 300 mm since the mosaic radius was only 325 mm. The radii vary within the limits:  $r_1 \in [80, 200]$ ,  $r_2 \in [100, 300]$ . An example of the distribution of a criterion parameter is shown in Fig. 12.

To find the best criterion, the following metric of separation errors by three masses was chosen. Theoretically, the lower the mass of the primary nuclei—the narrower the spot of Cherenkov light, so the higher the value of the criterion—the lighter the initial nuclei. Three classes were considered, e.g. two class separation boundaries— $p$ – $N$  and  $N$ – $Fe$ . The mini-

imum value of the maximum separation error for each of nuclei was taken as the main metric. For a classification error, the ratio of the number of incorrectly classified events relative to the calculated threshold was taken. As a result of procedure optimization, the following results were obtained: the  $p$ – $N$  separation boundary was 0.699 and resulted in 31.4% of falsely classified proton showers and the  $N$ – $Fe$  boundary was at 0.614 and resulted in 31.7% of falsely classified iron showers (see Fig. 13).

At the moment, the distribution is constructed without taking into account corrections for optical effects and background. In the future, this method will be refined and a two-dimensional criterion will be used to increase the separation accuracy.

### 5. DIRECT CHERENKOV LIGHT

Two similar approaches for estimating the EAS arrival direction were considered. One based on an angular distribution modeled using CORSIKA, the second used an angular distribution mediated by the detector—the Cherenkov image. In the first case, the results reflect the best accuracy that can be achieved using the method in question, in the second case they show what can be obtained from a certain form of the detector. In this particular case, as a model of a detector a biconvex lens focusing light on a position-sensitive photosensor (conventionally a CCD matrix) was used. The lens had a focal length of 11.28 cm and an area of 1 dm<sup>2</sup>, and the sensitive element was a 6 × 6 cm square.

Both when estimating the mass of the primary particle or EAS direction, the angular distribution and the Cherenkov image were analyzed in a similar way, what allowed to evaluate the maximum effectiveness of the method and understand what should be sought when modeling the real detector.

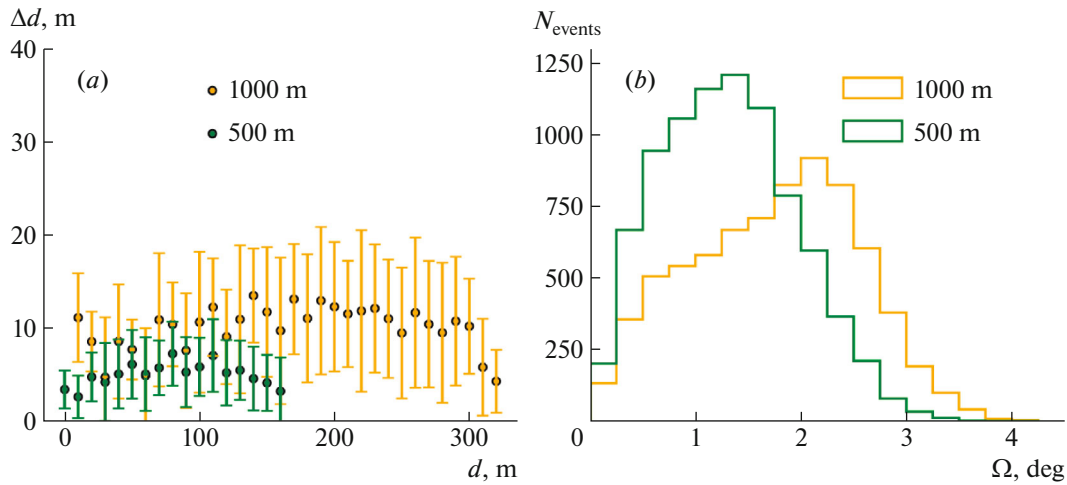


**Fig. 10.** (a) Dependence of the average axis location errors on the distance between the shower axis and the telescope axis for detector altitudes of 500 and 1000 m. (b) The distribution of EAS arrival direction estimation errors for the same two heights.

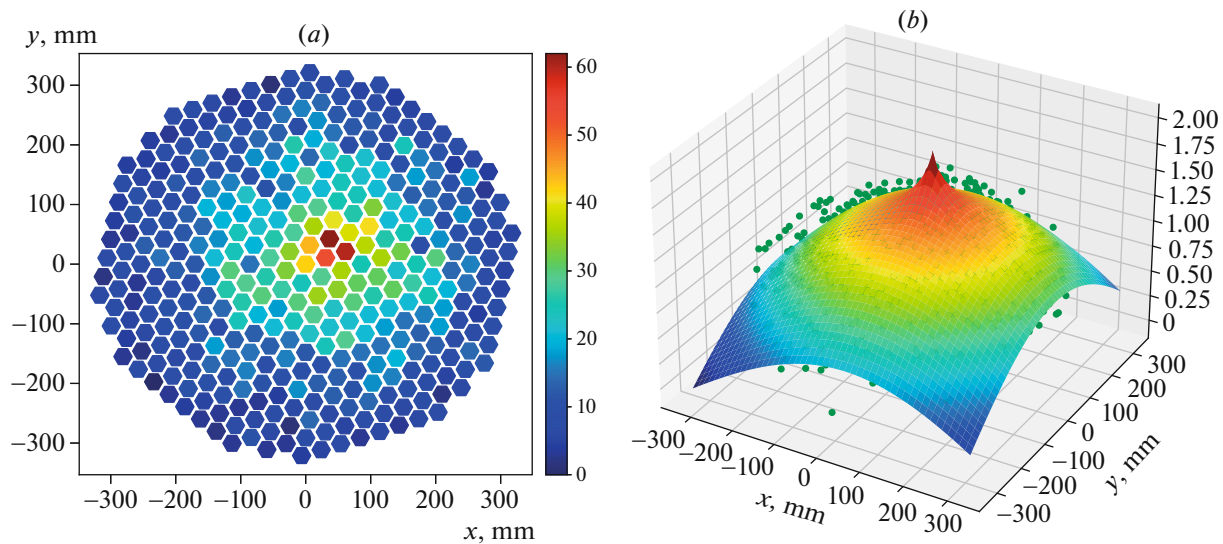


**Fig. 11.** An example of EAS Cherenkov photons LDF approximation for an event without background. (a) The number of photons per SiPM segment is presented by color (axes are in millimeters). (b) Photon counts from the left graph are shown as green dots. The surface is the LDF approximation.

### 5.1. EAS Arrival Direction

**5.1.1. Photons' Angular Distributions Analysis.** The angular distribution (as described above in the “Modelling” section) was simulated using a  $200 \times 200$  grid with a  $0.25^\circ \times 0.25^\circ$  cell. Such a grid is called “superfine” (other grid options are discussed below in the subsection “Grid effects”). The position of the detector relative to the shower axis was determined by the azimuth angle  $\psi$  and the distance  $R$ . The detector sees the shower from the side, so the spot of light in the field of view of the detector is oriented with its long axis pointing in the direction of the shower relative to the detector.

To estimate the arrival direction, the maximum or the centre of mass of the distribution can be used. In

this work we implemented both. The error in estimating the arrival direction is the angle between the real direction and the estimated one. In practice, all the points found are offset from the real direction along the large axis of the light distribution, as illustrated in Fig. 14.

The offset value depends on the distance to the shower and is different for these two methods. This allows us to improve the results by accounting for this offset. The method was used on 360 modelled EAS from different 10 PeV primary nuclei. Two detector positions were used (100 and 140 m). The results are presented in Table 4.

**5.1.2. Cherenkov Images Analysis.** The same dataset as above was used for this part. Same

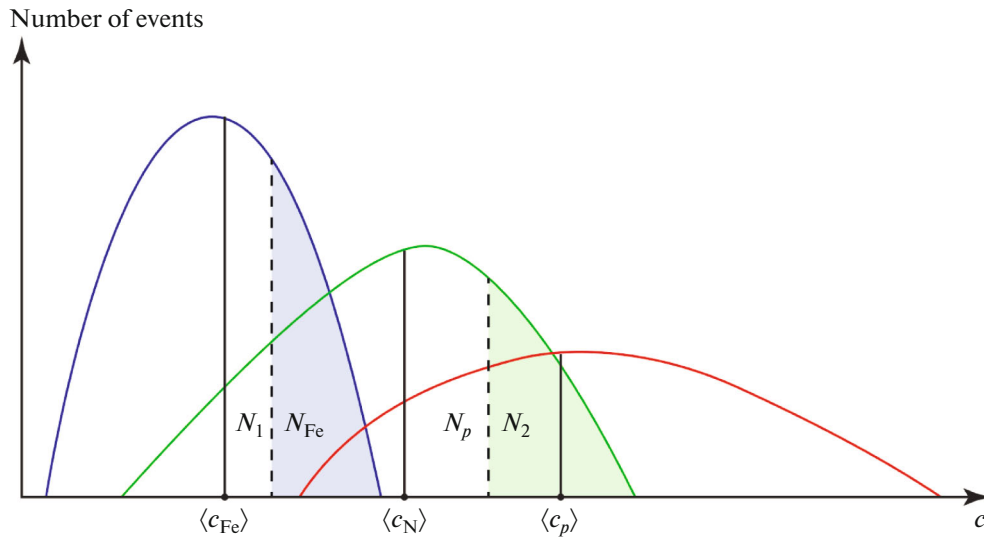


**Fig. 12.** A scheme of the nuclei class separation method. Values  $\langle c_p \rangle$ ,  $\langle c_N \rangle$ ,  $\langle c_{Fe} \rangle$  are the average values of the criterion for nuclei;  $N_2$  is the number of events from primary nitrogen nuclei that lie to the right of the  $p$ – $N$  classes boundary;  $N_p$  is the number of events from primary protons that lie to the left of that boundary. Same logic is applied to  $N_1$  and  $N_{Fe}$  values. The boundary varies within the domain  $[\langle c_N \rangle; \langle c_p \rangle]$  until equal classification errors are obtained for the pair of classes, that is, probabilities  $P\{p \rightarrow N\}$  and  $P\{N \rightarrow p\}$  are the same. The same is true for the  $N$ – $Fe$  pair.

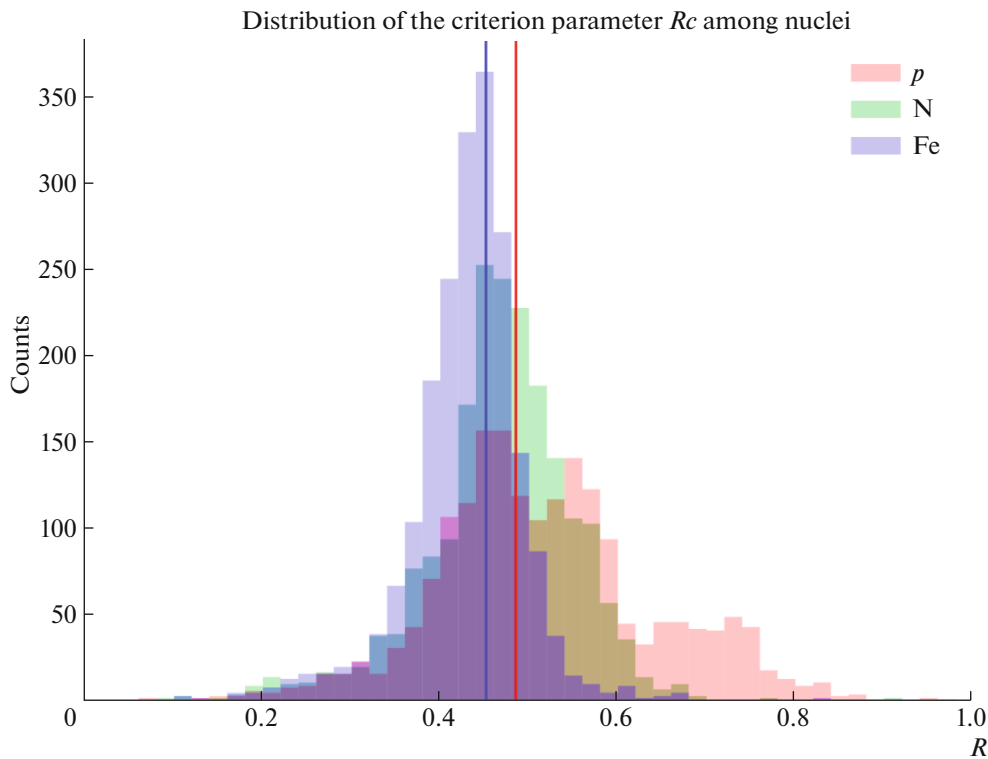


**Fig. 13.** A histogram of the criterion parameter distribution for 10 PeV showers with a  $10^\circ$  zenith angle for the detector flight altitude of 1000 m.

methods were used—position of the image maximum (brightest pixel) and centre of mass of the image. This allows to compare the results and evaluate the effects of the detector optics. The results of shower arrival

direction estimations for two methods are shown in Fig. 15.

By taking into account the systematic offset in the direction from the centre of mass to the maximum,

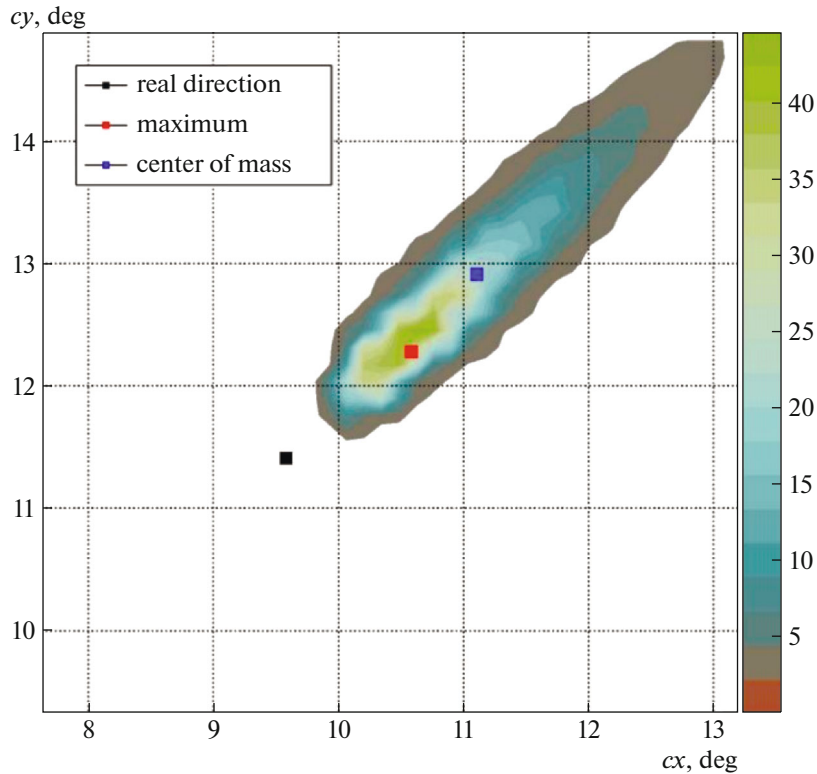


**Fig. 14.** Direct Cherenkov light distribution from a 10 PeV proton. Points indicate real EAS arrival direction (black), maximum (red) and distribution center of mass (blue).

the value of which depends on the distance from the shower axis, it is possible to achieve a  $0.2^\circ$  accuracy of the shower arrival direction estimation (see Table 5).

### 5.2. Primary Particle Mass Estimation Using Direct Cherenkov Light

Same as with arrival direction two approaches were used for EAS primary particle mass estimation to evaluate the detector effects on the data. One approach used modelled angular distribution, the other used the Cherenkov image.

At the moment, the Cherenkov light angular distribution parameters that are sensitive to the primary mass are screened. A number of parameters are known from the Cherenkov gamma-ray astronomy technique (for example, the Hillas parameters), but the task of separating primary nuclei by mass differs in formulation. There is a more subtle difference in the shape of the angular distributions from different nuclei than in the separation of gamma events, and there is no indication of the shower source, what makes the orientation angle of the image useless as a mass parameter.

Currently, the length of the angular distribution spot's or Cherenkov image's large axis is used to classify particles: when two nuclei groups are separated from each other the critical length of the large

axis is set and events with an axis length greater than the critical one belong to the light mass group, and shorter ones—to the heavier mass group. The ratio of the misclassified events in a pair to the total number of events caused by a particle is called a classification error and is a measure of the probability of misclassification of a particle. The quality of the criterion is assessed by classification errors: the smaller the error—the better the criterion.

The set of simulated EAS on the basis of which angular distributions and Cherenkov images were created had the following parameters:  $15^\circ$  zenith angle,  $50^\circ$  azimuth angle, 140 m from the shower axis. By analyzing the simulated events, it was found that the quality of separation is influenced by such factors as the azimuthal position of the detector relative to the shower axis (for both the angular distributions and images), the choice of the threshold type and value (for both the angular distributions and images), the choice of the grid step (analyzed only for angular distributions), the choice of the approximating function.

**5.2.1. Detector Position Effects.** Different variants of criteria based on the size of the long axis of the spot were tested:

1) integral: using a sample of different detector locations around the axis of the shower (uniform azimuth distribution);

**Table 4.** Shower arrival direction estimation errors (in degrees) using angular distribution

Distance to the shower axis	Maximum without offset correction	Centre of mass without offset correction	Maximum with offset correction	Centre of mass with offset correction
100 m	1.28	2.28	0.10	0.22
140 m	1.46	2.78	0.20	0.32

**Table 5.** Shower arrival direction estimation errors (in degrees) using images

Distance to the shower axis	Maximum without offset correction	Centre of mass without offset correction	Maximum with offset correction	Centre of mass with offset correction
100 m	1.2	1.7	0.12	0.16
140 m	1.4	2.0	0.14	0.19

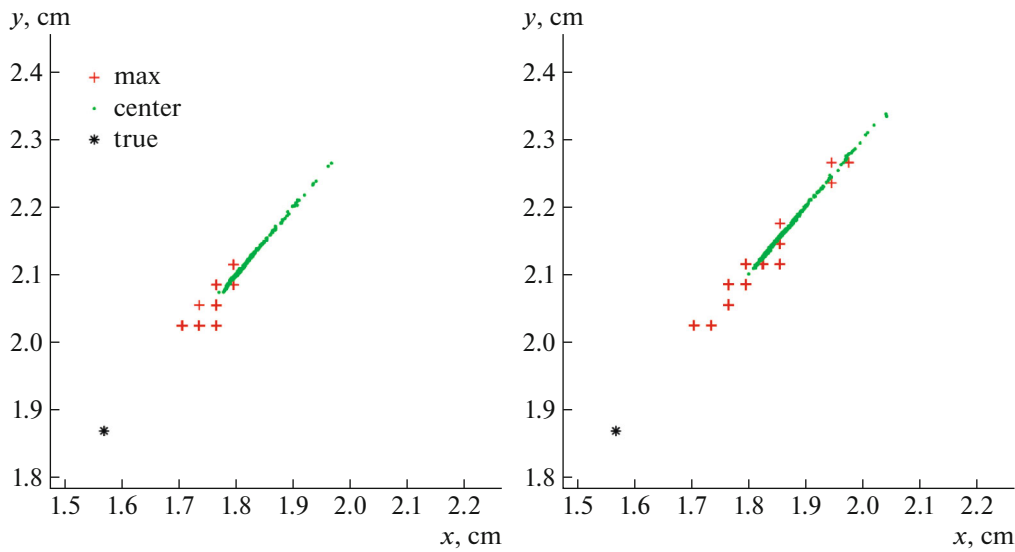


**Fig. 15.** Cherenkov light image centers from 10 PeV protons at distances 100 and 140 m from the shower axis. Points indicate the real EAS arrival direction (black), maximum (red) and distribution center of mass (blue).

2) integral within the quadrant: with sampling for uniformly distributed detector azimuths within the quadrant;

3) point-based: for several specific detector positions around the axis of the shower.

The distance from the axis of the shower to the detector in each case remained the same.

It was found that the degree of azimuth averaging affects the spot's long axis size distribution and the quality of EAS separation by mass. At the same time the quality of the quadrant integral criterion does not differ much from that of the full angle integral criterion. For a more accurate estimation of the primary mass, more precise information is needed about the detector position relative to the shower axis, which, in turn, can be obtained from the orientation angle of

the light spot on the detector mosaic. The orientation angle  $\Phi$  is the angle between the large axis of the spot and the positive direction of the  $X$  axis of the mosaic. In Fig. 16 the distribution of orientation angles for each azimuthal position of the detector is presented. Each position of the detector corresponds to its own range of orientation angles, and vice versa, each orientation angle corresponds to a certain range of the detector azimuths. It turned out that the azimuthal position of the detector  $\psi$  relative to the axis of the shower can be determined with sufficient accuracy from the angle  $\Phi$ , which allows to use a point-based criterion. According to our estimates, it is enough to know  $\psi$  with an accuracy of  $20^\circ-25^\circ$  to significantly (by 25–30%) reduce classification errors.

It was found that the position of the detector affects the classification errors, as shown in Table 6 and

**Table 6.** Errors in the classification of primary particles by mass depending on the azimuthal position of the detector  $\psi$ ; angular distributions, point-based criterion, absolute threshold, “fine” grid

$\psi$	Threshold	$p$ -N	N-Fe
5°	3	0.26	0.25
	7	0.32	0.37
27.5°	3	0.28	0.22
	7	0.45	0.34
50°	3	0.26	0.23
	7	0.31	0.47
72.5°	3	0.23	0.33
	7	0.24	0.46
95°	3	0.29	0.35
	7	0.30	0.32

Table 7, but the effect is not too great. Thresholds with minimal errors are selected.

**5.2.2. Threshold Type and Value.** The choice of a light spot or image processing threshold significantly affects the mass separation quality. The threshold was determined by analyzing the histogram of photon counts on the modelled grid. The absolute threshold was defined as a certain critical number

**Table 7.** Errors in the classification of primary particles by mass depending on the azimuthal position of the detector  $\psi$ ; Cherenkov images, point-based criterion, absolute threshold, “fine” grid

$\psi$	Threshold	$p$ -N	N-Fe
5°	5	0.34	0.31
	7	0.36	0.36
	8	0.33	0.35
32.5°	5	0.28	0.26
	7	0.30	0.29
	8	0.32	0.31
50°	5	0.27	0.27
	7	0.25	0.31
	8	0.26	0.32
77.5°	5	0.39	0.39
	7	0.34	0.34
	8	0.38	0.32
95°	5	0.35	0.38
	7	0.36	0.32
	8	0.36	0.38

of photons in a cell, and the relative threshold was defined as a fraction of the largest number of photons in a single cell of the distribution. During analysis, only cells whose contents exceeded the threshold were considered. When using an absolute threshold, the separation is significantly better and therefore it will be used further.

Since the cell size for the angular distribution is fixed at CORSIKA simulation level and for the Cherenkov image it is selected at the processing stage, the same absolute thresholds may correspond to different photon densities. For example, if the cell size of the image histogram is 0.12 cm, the angular cell size is 0.6°, that is, the threshold of 5 photoelectrons per cell for the image corresponds to 0.77 photoelectrons per cell for the angular distribution.

For comparison in Table 8 and Table 9 the “fine” grid was used, the azimuthal position of the detector  $\psi = 50^\circ$ . The “fine” grid is used everywhere for Cherenkov images.

**5.2.3. Grid Effects.** The detail level of the Cherenkov light angular distribution modelled by CORSIKA affects the quality of primary particle mass separation quality: if, instead of a “fine” grid with a cell size of 0.5°, a “superfine” grid with a cell size of 0.25° is used, classification errors will significantly decrease. When using an “ultrafine” grid with a 0.2° cell size, classification errors become even smaller. For the azimuthal position of the detector  $\psi = 50^\circ$  and shower axis distance of 140 m the comparison is presented in Table 10.

**Table 8.** Classification errors for different absolute threshold values for angular distributions

Absolute threshold			Relative threshold		
value	$p$ -N	N-Fe	value	$p$ -N	N-Fe
2	0.25	0.26	0.03	0.30	0.38
3	0.26	0.23	0.05	0.43	0.43
5	0.23	0.29	0.07	0.33	0.62

**Table 9.** Classification errors for different absolute threshold values for Cherenkov images

Absolute threshold			Relative threshold		
value	$p$ -N	N-Fe	value	$p$ -N	N-Fe
3	0.32	0.32	0.03	0.36	0.38
5	0.27	0.27	0.05	0.35	0.32
7	0.25	0.31	0.07	0.32	0.36

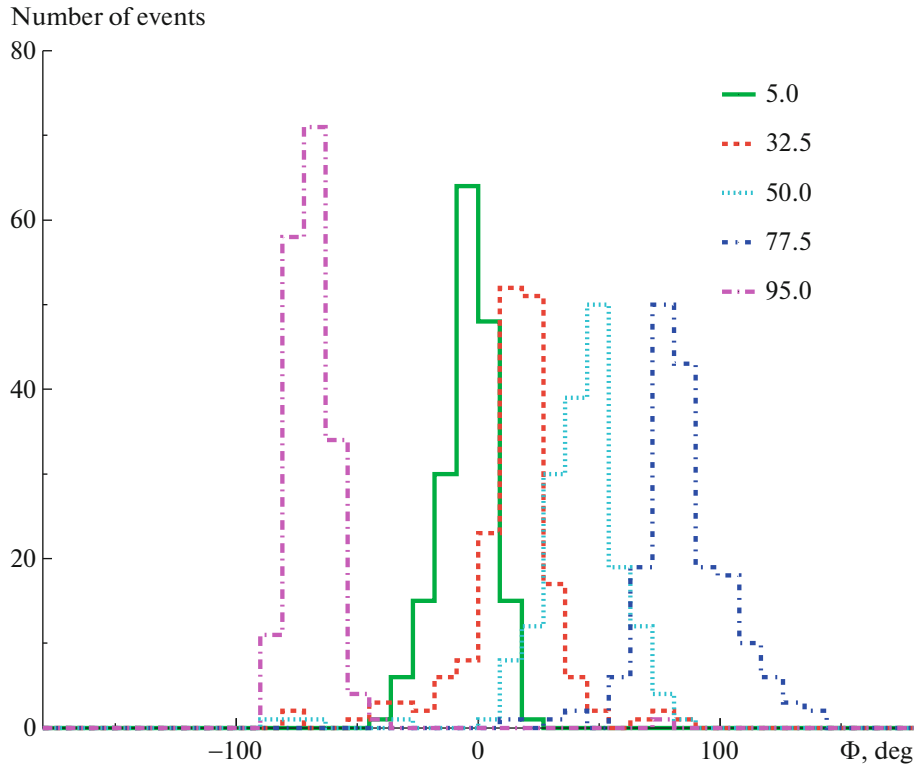


Fig. 16. Classification errors based on the orientation angle of the azimuthal positions of the detector in degrees relative to the EAS axis for angular images.

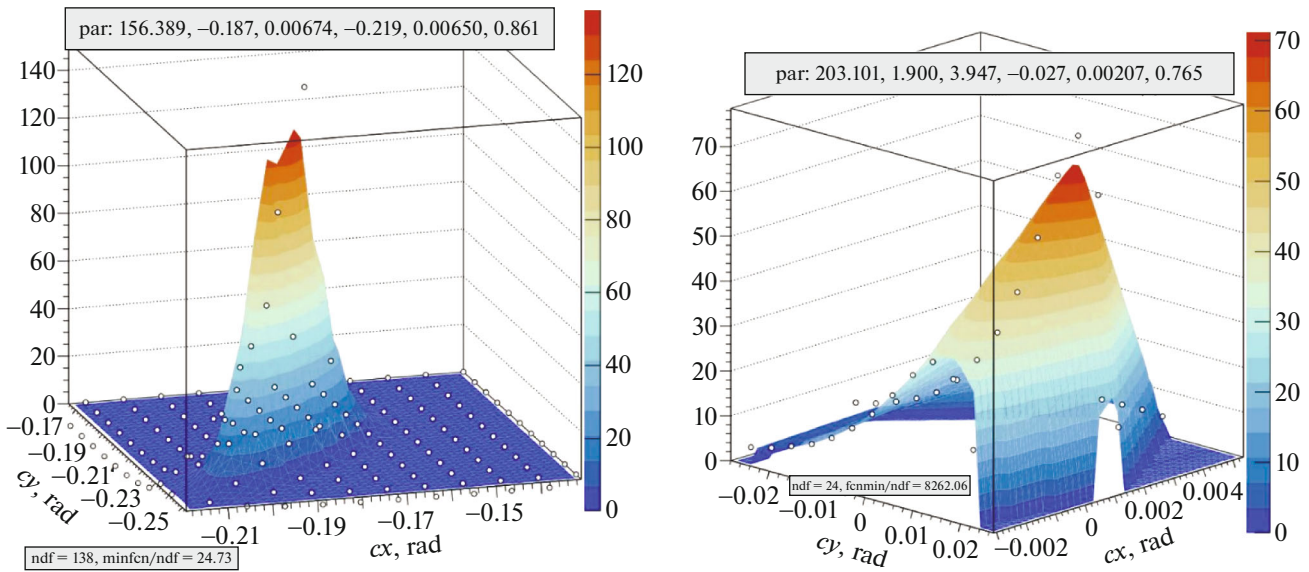


Fig. 17. Approximation of the angular distributions by a two-dimensional Gaussian distribution (a) and a copula function (b).

It can be seen that the separation quality improves with increasing grid resolution. This means that the “fine” and “superfine” grids cannot describe all the details of the angular distribution, therefore, it is necessary to use the “ultrafine” grid. The comparison was carried out for angular distributions, the situation

for Cherenkov images requires additional research, but we expect the same trend.

**5.2.4. The Use of Approximation.** The length of the light distribution’s long axis can be calculated not only by the distribution moments, as implemented above, but also by approximating the an-

**Table 10.** Classification errors table for different grid resolutions

Absolute threshold value	Fine		Superfine		Ultrafine	
	<i>p</i> -N	N-Fe	<i>p</i> -N	N-Fe	<i>p</i> -N	N-Fe
3	0.26	0.23	0.25	0.22	0.24	0.16
7	0.31	0.47	0.27	0.17	0.19	0.20
10	0.52	0.35	0.30	0.25	0.21	0.24

gular distribution or Cherenkov image with some two-dimensional function. At the moment, analysis has been performed using a two-dimensional Gaussian distribution as an approximating function (see Fig. 17a).

Currently, classification errors for this approach in most cases reach values of 0.6 or more, indicating that such analysis does not allow good separation. This is due to the discrepancy between the maximum of the distribution and the centre of the spot, what complicates the approximation process: in order to describe such a peak shape, it is necessary to resort to asymmetric functions such as beta and gamma distributions. At the moment we are in search of a suitable function, and one of the options is shown in Fig. 17b—the normal distribution over the variable  $x$  is connected with the gamma distribution over  $y$  using a normal copula function.

For asymmetrical distributions, it is also possible to introduce the concept of the length of the major axis, but we expect to obtain from them other parameters sensitive to the primary mass. It is important that having a good approximation of the distribution or image a more conscious approach to the choice of such parameters is possible.

## 6. CONCLUSIONS

The design of the new detector is optimized for solving the problem of the primary cosmic rays' mass composition. The main detector is a reflected light telescope, as it allows to evaluate all of the primary parameters of a shower. The new configuration of the reflected Cherenkov light telescope for the SPHERE-3 detector makes it possible to achieve an optical resolution of the order of 10 mm with a wide solid angle of registration up to  $\pm 20$  degrees. The principles of operation and construction of measuring electronics, trigger system and SiPM segments in the detector mosaic are determined.

A special feature of the new detector is an additional direct Cherenkov light detector that analyses its angular distribution and allows to estimate the

shower arrival direction and mass of the primary particle. The information capabilities of the Cherenkov light angular distribution and its images in a simple version of the detector are considered. A number of methodological issues of the modelling procedure and analysis methods of the angular distribution and its images have been solved.

Information richness of the angular distribution of Cherenkov light is considered in two ways. First, the angular distribution given by the CORSIKA code is studied for its sensitivity to the primary mass. Second, the images of the angular distribution from a simple detector are considered in this regard. In both cases certain sensitivity is found.

Direct Cherenkov light is also found capable of defining the shower axis direction with an uncertainty of about 0.5 degree. Still the reflected light telescope remains the main detector since the primary energy estimation relies on it.

In order to solve the PCR mass composition problem, it is important to ensure the high probability of detection by both telescopes, what will significantly increase the accuracy of the primary parameters' estimations due to independent data sets provided by them.

## ACKNOWLEDGEMENTS

The research was carried out using the equipment of the shared research facilities of HPC computing resources at Lomonosov Moscow State University [22].

## FUNDING

This work was supported by the Russian Science Foundation, grant no. 23-72-00006, <https://rscf.ru/project/23-72-00006/>.

## CONFLICT OF INTEREST

The authors of this work declare that they have no conflicts of interest.

## REFERENCES

1. S. Thoudam, J. P. Rachen, A. van Vliet, A. Achterberg, S. Buitink, H. Falcke, and J. R. Hörandel, *Astron. Astrophys.* **595**, A33 (2016). <https://doi.org/10.1051/0004-6361/201628894>
2. F. Schroeder, T. AbuZayyad, L. Anchordoqui, K. Andeen, X. Bai, S. BenZvi, D. Bergman, A. Coleman, H. Dembinski, M. DuVernois, T. Gaisser, F. Halzen, A. Haungs, J. Kelley, H. Kolanoski, F. McNally, M. Roth, F. Sarazin, D. Seckel, R. Smida, D. Soldin, and D. Tosi, *Bulletin of the AAS* **51**, 131 (2019). <https://baas.aas.org/pub/2020n3i131>.

3. F. G. Schröder, in *Proceedings of 36th International Cosmic Ray Conference—PoS(ICRC2019)*, Proc. Sci., Vol. 358 (Sissa Medialab, 2019), p. 30.  
<https://doi.org/10.22323/1.358.0030>
4. P. A. Collab., Phys. Lett. B **762**, 288 (2016).  
<https://doi.org/10.1016/j.physletb.2016.09.039>
5. A. V. Glushkov and A. V. Saburov, JETP Lett. **98**, 589 (2014).  
<https://doi.org/10.1134/s0021364013230057>
6. W. D. Apel, J. C. Arteaga-Velázquez, K. Bekk, M. Bertaina, J. Blümer, H. Bozdog, I. M. Brancus, E. Cantoni, A. Chiavassa, F. Cossavella, K. Daumiller, V. de Souza, F. Di Pierro, P. Doll, R. Engel, J. Engler, M. Finger, B. Fuchs, D. Fuhrmann, H. J. Gils, R. Glasstetter, C. Grupen, A. Haungs, et al. (The KASCADE-Grande Collaboration), Astropart. Phys. **47**, 54 (2013).  
<https://doi.org/10.1016/j.astropartphys.2013.06.004>
7. D. Kang, W. D. Apel, J. C. Arteaga-Velázquez, K. Bekk, M. Bertaina, J. Blümer, H. Bozdog, E. Cantoni, A. Chiavassa, F. Cossavella, K. Daumiller, V. De Souza, F. Di Pierro, P. Doll, R. Engel, D. Fuhrmann, A. Gherghel-Lascu, H. J. Gils, R. Glasstetter, C. Grupen, A. Haungs, D. Heck, J. R. Hörandel, T. Huege, K.-H. Kampert, H. O. Klages, K. Link, P. Łuczak, H. J. Mathes, H. J. Mayer, J. Milke, C. Morello, J. Oehlschläger, S. Ostapchenko, T. Pierog, H. Rebel, D. Rivera-Rangel, M. Roth, H. Schieler, S. Schoo, F. G. Schröder, O. Sima, G. Toma, G. C. Trincherro, H. Ulrich, A. Weindl, J. Wochele, and J. Zabierowski, in *Proceedings of 37th International Cosmic Ray Conference—PoS(ICRC2021)*, Proc. Sci., Vol. 395 (Sissa Medialab, 2021), p. 313.  
<https://doi.org/10.22323/1.395.0313>
8. D. Kostunin, I. Plokhikh, M. Ahlers, V. Tokareva, V. Lenok, P. A. Bezyazeev, S. Golovachev, V. Sotnikov, R. Mullyadzhyanov, and E. Sotnikova, in *Proceedings of 37th International Cosmic Ray Conference—PoS(ICRC2021)*, Proc. Sci., Vol. 395 (Sissa Medialab, 2021), p. 319.  
<https://doi.org/10.22323/1.395.0319>
9. T. Antoni, W. D. Apel, A. F. Badea, K. Bekk, A. Bercuci, J. Blümer, H. Bozdog, I. M. Brancus, A. Chilingarian, K. Daumiller, P. Doll, R. Engel, J. Engler, F. Feßler, H. J. Gils, R. Glasstetter, A. Haungs, D. Heck, J. R. Hörandel, K.-H. Kampert, H. O. Klages, G. Maier, H. J. Mathes, H. J. Mayer, J. Milke, M. Müller, R. Obenland, J. Oehlschläger, S. Ostapchenko, M. Petcu, H. Rebel, A. Risse, M. Risse, M. Roth, G. Schatz, H. Schieler, J. Scholz, T. Thouw, H. Ulrich, J. van Buren, A. Vardanyan, A. Weindl, J. Wochele, and J. Zabierowski (KASCADE Collaboration), Astropart. Phys. **24**, 1 (2005).  
<https://doi.org/10.1016/j.astropartphys.2005.04.001>
10. M. G. Aartsen, R. Abbasi, Y. Abdou, M. Ackermann, J. Adams, J. A. Aguilar, M. Ahlers, D. Altmann, J. Auffenberg, X. Bai, M. Baker, S. W. Barwick, V. Baum, R. Bay, J. J. Beatty, S. Bechet, J. Becker Tjus, K.-H. Becker, M. L. Benabderrahmane, S. BenZvi, P. Berghaus, D. Berley, E. Bernardini, A. Bernhard, D. Bertrand, D. Z. Besson, G. Binder, D. Bindig, M. Bissok, E. Blaufuss, J. Blumenthal, D. J. Boersma, S. Bohaichuk, C. Bohm, D. Bose, et al. (IceCube Collaboration), Phys. Rev. D **88**, 42004 (2013).  
<https://doi.org/10.1103/physrevd.88.042004>
11. D. Soldin (The IceCube Collaboration), in *Proceedings of 36th International Cosmic Ray Conference—PoS(ICRC2019)*, Proc. Sci., Vol. 358 (Sissa Medialab, 2019), p. 14.  
<https://doi.org/10.22323/1.358.0014>
12. H. Dembinski, R. Engel, A. Fedynitch, T. Gaisser, F. Riehn, and T. Stanev, in *Proceedings of 35th International Cosmic Ray Conference—PoS(ICRC2017)*, Proc. Sci., Vol. 301 (Sissa Medialab, 2017), p. 533.  
<https://doi.org/10.22323/1.301.0533>
13. E. A. Bonvech, D. V. Chernov, V. S. Latypova, C. Azra, V. I. Galkin, V. A. Ivanov, D. A. Podgrudkov, and T. M. Roganova, Bull. Russ. Acad. Sci.: Phys. **88**, 435 (2024).  
<https://doi.org/10.1134/s1062873823705676>
14. V. I. Galkin, A. S. Borisov, R. Bakhromzod, V. V. Ba-traev, S. Latipova, and A. Muqumov, EPJ Web Conf. **145**, 15004 (2017).  
<https://doi.org/10.1051/epjconf/201614515004>
15. E. A. Bonvech, C. J. Azra, D. V. Chernov, V. I. Galkin, E. L. Entina, V. A. Ivanov, V. S. Latypova, D. A. Podgrudkov, T. M. Roganova, and M. D. Ziva, Phys. At. Nucl. **86**, 1048 (2023).  
<https://doi.org/10.1134/s1063778824010149>
16. D. Heck, J. Knapp, J. N. Capdevielle, G. Schatz, and T. Thouw, Rep. FZKA (Forschungszentrum Karlsruhe, Karlsruhe, 1998), p. 6019.  
<https://doi.org/10.5445/IR/270043064>
17. D. V. Chernov, C. Azra, E. A. Bonvech, V. I. Galkin, V. A. Ivanov, V. S. Latypova, D. A. Podgrudkov, and T. M. Roganova, Phys. At. Nucl. **85**, 641 (2022).  
<https://doi.org/10.1134/s1063778822060059>
18. C. M. Poole, I. Cornelius, J. V. Trapp, and C. M. Langton, Australas. Phys. Eng. Sci. Med. **35**, 329 (2012).  
<https://doi.org/10.1007/s13246-012-0159-8>
19. D. A. Podgrudkov, E. A. Bonvech, I. V. Vaiman, D. V. Chernov, I. I. Astapov, P. A. Bezyazeev, M. Blank, A. N. Borodin, M. Brückner, N. M. Budnev, A. V. Bulan, A. Vaidyanathan, R. Wischnewski, P. A. Volchugov, D. M. Voronin, A. R. Gafarov, O. A. Gress, T. I. Gress, O. G. Grishin, A. Yu. Garmashi, V. M. Grebenyuk, A. V. Grinyuk, A. N. Dyachok, D. P. Zhurov, A. V. Zagorodnikov, A. L. Ivanova, N. N. Kalmykov, V. V. Kindin, S. N. Kiryuhin, R. L. Kokoulin, K. G. Kompaniets, E. E. Korosteleva, V. A. Kozhin, et al., Bull. Russ. Acad. Sci.: Phys. **85**, 408 (2021).  
<https://doi.org/10.3103/s1062873821040286>

20. A. A. Amineva, A. V. Pantyuhin, and D. A. Podgrudkov, *Uchenye Zapiski Fizicheskogo Fakul'teta Moskovskogo Gosudarstvennogo Universiteta*, No. 4, 2341602 (2023).  
<http://uzmu.phys.msu.ru/abstract/2023/4/2341602/>.
21. V. S. Latypova and V. I. Galkin, *Uchenye Zapiski Fizicheskogo Fakul'teta Moskovskogo Gosudarstvennogo Universiteta*, No. 4, 2341604 (2023).
22. V. V. Voevodin, A. S. Antonov, D. A. Nikitenko, P. A. Shvets, S. I. Sobolev, I. Yu. Sidorov, K. S. Stefanov, V. V. Voevodin, and S. A. Zhumatiy, *Supercomputing Frontiers and Innovations* **6** (2), 4 (2019).  
<https://doi.org/10.14529/jsfi190201>

**Publisher's Note.** Pleiades Publishing remains neutral with regard to jurisdictional claims in published maps and institutional affiliations.

AI tools may have been used in the translation or editing of this article.